RESEARCH ARTICLE

Key Points:

- Velocity pulsing is ubiquitous in continuous turbidity currents in Lillooet Lake and Xiaolangdi Reservoir, even though the river input is steady
- Stability analysis of numerical, laboratory, and field data indicates that both Rayleigh-Taylor and Kelvin-Helmholtz instabilities can cause pulsing
- Rayleigh-Taylor instabilities result from river mouth lobes and have higher bulk Richardson numbers and smaller periods than Kelvin-Helmholtz instabilities

On the Causes of Pulsing in Continuous Turbidity Currents

Ray Kostaschuk[1] [ID]**, Mohamad M. Nasr-Azadani[2], Eckart Meiburg[2]** [ID]**, Taoyuan Wei[3], Zhongyuan Chen[3], Maria Eletta Negretti[4], Jim Best[5]** [ID]**, Jeff Peakall[6], and Daniel R. Parsons[7]** [ID]

[1]River Dynamics Research Group, Department of Geography, Simon Fraser University, Burnaby, British Columbia, Canada, [2]Department of Mechanical Engineering, University of California, Santa Barbara, CA, USA, [3]State Key Laboratory of Estuarine and Coastal Research, East China Normal University, Shanghai, China, [4]Laboratoire des Ecoulements Géophysiques et Industriels, UMR 5519 CNRS/UGA/INPG, Grenoble Cedex 9, France, [5]Departments of Geology, Geography and GIS, Mechanical Science and Engineering, and Ven Te Chow Hydrosystems Laboratory, University of Illinois at Urbana-Champaign, Urbana, IL, USA, [6]School of Earth and Environment, University of Leeds, Leeds, UK, [7]Department of Geography, Environment and Earth Sciences, University of Hull, Hull, UK

Abstract Velocity pulsing has previously been observed in continuous turbidity currents in lakes and reservoirs, even though the input flow is steady. Several different mechanisms have been ascribed to the generation of these fluctuations, including Rayleigh-Taylor (RT) instabilities that are related to surface lobes along the plunge line where the river enters the receiving water body and interfacial waves such as Kelvin-Helmholtz instabilities. However, the understanding of velocity pulsing in turbidity currents remains limited. Herein we undertake a stability analysis for inclined flows and compare it against laboratory experiments, direct numerical simulations, and field data from Lillooet Lake, Canada, and Xiaolangdi Reservoir, China, thus enabling an improved understanding of the formative mechanisms for velocity pulsing. Both RT and Kelvin-Helmholtz instabilities are shown to be prevalent in turbidity currents depending on initial conditions and topography, with plunge line lobes and higher bulk Richardson numbers favoring RT instabilities. Other interfacial wave instabilities (Holmboe and Taylor-Caulfield) may also be present. While this is the most detailed analysis of velocity pulsing conducted to date, the differences in spatial scales between field, direct numerical simulations, and experiments and the potential complexity of multiple processes acting in field examples indicate that further work is required. In particular, there is a need for simultaneous field measurements at multiple locations within a given system to quantify the spatiotemporal evolution of such pulsing.

Plain Language Summary Turbidity currents are dense mixtures of sediment and water that flow along the bottoms of lakes, reservoirs, and oceans. Deposits of turbidity currents can provide a continuous record of climate variations, form submarine fans and abyssal plains, two of the largest sediment features on Earth, and create economically important sources for oil and gas. Turbidity currents supply nutrients and oxygen to deep ocean and lake basins and are the primary cause of deposition and loss of storage capacity in water reservoirs. Turbidity currents that are driven by prolonged river flow and constant supplies of suspended sediment are referred to as *continuous turbidity currents* and can flow for weeks to months. Continuous turbidity currents are characterized by regular fluctuations in velocity or *pulsing* even though the river inflow does not fluctuate. This study examines the causes of pulsing and is of practical importance because pulsing increases mixing between the river and lake or ocean and produces distinct features in the rock record.

1. Introduction

Turbidity currents are sediment-laden underflows that enter less dense bodies of water and flow downward along the bed until their sediment load is deposited and neutral buoyancy is reached (see Meiburg & Kneller, 2010, for a recent review). Turbidity currents are initiated by one or more processes such as landslides, debris flows, mine tailings disposal, seismic-induced subaqueous slumps, and increased river discharge (Normark, 1989). These flows are important mechanisms for sediment transport and deposition in subaqueous environments and are capable of distributing substantial amounts of sediment across great distances and forming distinctive deposits in deep and distal locations (Desloges & Gilbert, 1994; Weirich, 1986). Deposits of turbidity currents can provide a continuous record of climatic and catchment conditions (Crookshanks & Gilbert,
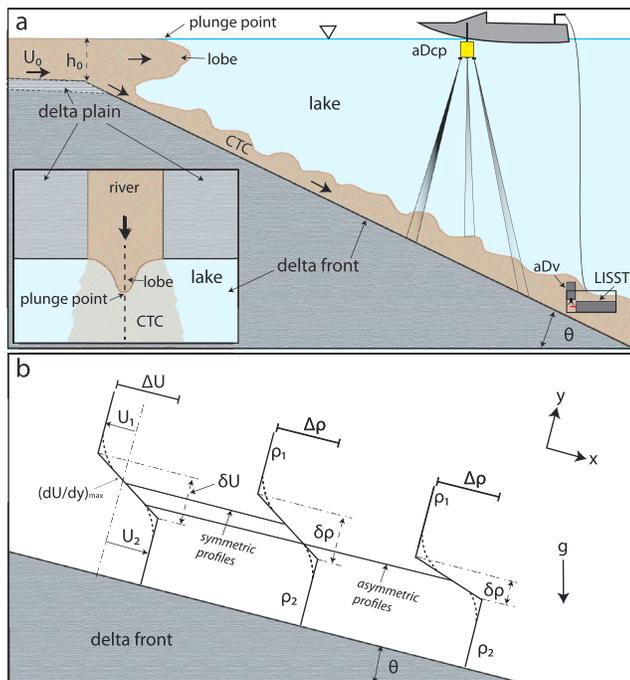
Figure 1. Definition diagrams. (a) Continuous turbidity current (CTC) generated by a river entering a lake and related field measurements. U_0 is the mean velocity at the outlet, h_0 is the depth at the outlet, θ is delta front slope, aDcp is acoustic Doppler current profiler, aDv is acoustic Doppler velocimeter, and LISST is laser in situ sediment transmissometer. A planform of the river mouth region is shown on the inset. (b) Velocity and density profiles for piecewise stability analysis of inclined flows, modified from Negretti et al. (2008, their Figure 2). $\Delta U = U_2 - U_1$ is the velocity difference over the profile, U_2 is the velocity of the CTC, U_1 is the velocity of the return flow, $(dU/dy)_{max}$ is the maximum value of the velocity gradient in the shear layer, δU is the thickness of the shear layer, $\Delta\rho = \rho_2 - \rho_1$ is the density difference over the profile, ρ_2 is the density of the CTC, ρ_1 is the density of the ambient lake water, and $\delta\rho$ is the thickness of the density layer.

2008) and are linked to the formation of submarine fans and abyssal plains, two of the largest sediment features on Earth (Bradford et al., 1997; Middleton, 1993), which may subsequently form economically important hydrocarbon reservoirs. Turbidity currents are also vital in nutrient cycling (Eadie et al., 2002), oxygenating deep oceanic and lacustrine basins (Hsu & Kelts, 1985; Lambert & Luthi, 1977), and are the primary cause of sedimentation and loss of storage capacity in water reservoirs (De Cesare et al., 2001).

Turbidity currents that are driven by prolonged river flow and constant supplies of suspended sediment are often referred to as *continuous turbidity currents* and can persist for long periods (Figure 1a). For instance, continuous turbidity currents have been documented in Lake Luzzone (De Cesare et al., 2001) and Lake Lugano (De Cesare et al., 2006) in Switzerland, Lake Ohau in New Zealand (Cossu et al., 2015), Lillooet Lake in Canada (Best et al., 2005; Desloges & Gilbert, 1994; Gilbert, 1975; Gilbert et al., 2006; Menczel & Kostaschuk, 2013), and the Xiaolangdi Reservoir on the Huanghe (Yellow) River in China (Wei, 2010; Wei et al., 2013). Studies in the Congo Canyon in the Atlantic Ocean (Azpiroz-Zabala et al., 2017) show that weeklong turbidity currents can develop, not directly from river flow but from an erosive front that feeds sediment to an expanding trailing body.

Best et al. (2005) were the first to measure whole field dynamics of continuous turbidity currents in their study of Lillooet Lake, and they found that, even though the river inflow was steady, there was a distinct *pulsing* in the velocity structure. Such pulsing is likely to enhance mixing between the influent and ambient water (Lawrence et al., 2013) and produce spatial variations in bed erosion and deposition that may result in a complex signature in the geological record (Lamb et al., 2010; Lamb & Mohrig, 2009).

Processes at the *plunge point* (Figure 1a), where river outflow initially passes underneath the ambient basin water, have been proposed as a mechanism for velocity pulsing. Best et al. (2005) suggest that pulses may be due to shifting positions of plunge line *lobes* at the river mouth (Figure 1a). Dai (2008) expanded on this interpretation by proposing that the pulses may be explained as a turbulent Rayleigh-Taylor (RT) instability. The RT instability occurs during *negative buoyancy* where the bottom surface of a layer of a denser fluid overlies lighter fluid in the presence of a gravitational field. In the turbulent RT instability, the fluid in the upper layer is turbulent at the onset of the instability and as such is governed by the eddy viscosity (Chakraborty et al., 2006). Dai (2008) proposed that RT instabilities would result from the negatively buoyant lobes at the river mouth that are generated by the momentum of the flow as it enters the lake. These lobes extend offshore then sink to the bed, producing a *pulse* in the turbidity current. This process then repeats itself, resulting in a shift in the position of the lobes and hence pulsing underflows.

Pulsing can also result from stratified shear flow instabilities. If the shear across the interface of a stratified flow, such as a continuous turbidity current (Figure 1a), is strong enough to overcome the stabilizing effect of the stratification, instability leads to the development of large-amplitude, wave-like structures such as Kelvin-Helmholtz (KH; Brown & Roshko, 1974), Holmboe (H; Smyth et al., 2007; Smyth & Winters, 2003) and Taylor-Caulfield (TC; Carpenter et al., 2010; Caulfield et al., 1995; Guha & Lawrence, 2014; Taylor, 1931) instabilities. The profile of the density layer for the TC instability is composed of two distinct *steps* from high to low density, as opposed to single steps in the KH and H density profiles (Guha & Lawrence, 2014). Linear stability analysis is the classical temporal approach to assessing the interfacial stability of a flow (see Carpenter et al., 2011, for a recent review), and it examines the impact of small disturbances, or perturbations, on a background flow state. If the perturbations grow over time, this indicates that the background state is unstable and a different type of flow emerges. Perturbations are taken to be sinusoidal in the along-flow direction,

and their evolution in time is tracked. In the case of stratified shear flow, the background state corresponds to the basic vertical profiles of horizontal velocity and density (Figure 1b). The KH instability travels at the mean flow velocity, whereas the H instability is composed of two disturbances that grow at the same rate: a *positive* wave cusping into the upper layer and traveling to the right with respect to the mean flow and a *negative* wave cusping into the lower layer and traveling to the left with respect to the mean flow. When the velocity and density profiles are *asymmetric*, such that they are displaced vertically with respect to each other (Figure 1b), a *hybrid* or *one-sided* instability may result (Lawrence et al., 2013). For hybrid instabilities, the *cusping* of the H instability occurs on only one side of the interface, such as in experiments of fresh water over salt water (Lawrence et al., 1991). Unless the flow is forced at a frequency that favors the negative wave, the positive wave will dominate. Hybrid instabilities can exhibit complex behavior and cause more mixing than either the KH or H instability alone (Lawrence et al., 2013).

Most linear stability analyses of stratified shear flows are based on the classic Taylor-Goldstein equation for horizontal flows and ignore the influence of bed slope (θ: Figure 1), a parameter that is critical to understanding natural continuous turbidity currents. Negretti et al. (2008) focused on the role of bed slope using linear stability analysis of the two-dimensional momentum equations, written in a coordinate system in which the longitudinal direction is parallel to the sloping bottom and the vertical direction is orthogonal to the bed (Figure 1b). Instabilities are assumed to grow faster than the flow acceleration time scale caused by the inclined bed and although H instabilities were found, their temporal amplification rate was less than the acceleration due to the slope. Thus, only KH instability was examined in their analysis, with the flow becoming increasingly unstable as the bed slope steepened.

In the present study, we examine the causes of pulsing in continuous, natural turbidity currents in Lillooet Lake and Xiaolangdi Reservoir using laboratory experiments, direct numerical simulation (DNS), and field measurements. Although combining these diverse sets of data is challenging, the results provide unique insights into the generation of pulsing density underflows. The laboratory and DNS detail the structure of KH waves under highly controlled conditions, serving as a basis for comparison to the more variable field flows. Our analyses indicate that pulsing in Lillooet Lake, where plunge line lobes are common, is consistent with RT instability. In contrast, surface lobes are not obvious in the Xiaolangdi Reservoir and KH instability is the dominant pulsing mechanism.

2. Materials and Methods

2.1. DNS

The simulation software TURBINS (see Nasr-Azadani & Meiburg, 2011, 2014a; Nasr-Azadani et al., 2013, for details) is employed to perform DNSs of continuous gravity and turbidity currents. TURBINS is a highly parallel, finite difference-based computational fluid dynamics code that solves the Navier-Stokes equations using a Boussinesq approximation to describe the motion of the suspension, along with a transport equation for the sediment concentration field. The sediment grains are assumed to be sufficiently small so that their inertia is negligible and they move with the fluid velocity, onto which the Stokes settling velocity is superimposed (Necker et al., 2002). Complex topography is accounted for via an immersed boundary method (Mittal & Iaccarino, 2005).

The software TURBINS can be used for both two-dimensional (2-D) and three-dimensional (3-D) simulations (Nasr-Azadani & Meiburg, 2014a, 2014b). We chose 2-D simulations in this study for several reasons. Computational cost is much lower for 2-D than for 3-D, allowing us to explore the roles of bed configuration and sediment size in more detail in 2-D. In addition, TURBINS 3-D simulations are not fully 3-D in that they have lateral boundaries and the flow is not allowed to expand fully downstream, so 2-D slices within the 3-D simulations are comparable to those from 2-D simulations, although 2-D tends to generate stronger coherent structures compared to 3-D (Nasr-Azadani & Meiburg, 2014a). The narrow flume tank used in our laboratory experiment results in limited lateral expansion of the flow as well, so a 2-D DNS is comparable with the laboratory flow. Field flows in this study are essentially 2-D: the Xiaolangdi Reservoir density underflows are laterally confined by a subaqueous channel (Wei, 2010; Wei et al., 2013) and cross-flow measurements in Lillooet Lake show little lateral expansion of the flows over the short offshore distances in our measurements (Menczel & Kostaschuk, 2013).

Two-dimensional DNS were conducted for a combination of straight and segmented bed slopes, for gravity currents with no sediment, and for turbidity currents containing sediment with settling velocities consistent with sand (150 μm) and silt clay (30 μm)-sized particles. Dimensionless settling velocities are 0.15 (30% mass fraction) for the sand and 0.0043 (70% mass fraction) for the silt clay. The sand simulations showed that the sediment is deposited close to the river mouth and did not contribute significantly to the turbidity currents, which is consistent with field results (e.g., Menczel & Kostaschuk, 2013). The silt clay simulations were qualitatively similar to those of the gravity currents without sediment, so herein we examine gravity currents with zero settling velocity over a single bed slope of 11° beyond the river mouth, a gradient typical of steeper delta fronts such as at Lillooet Lake. The choice of gravity current simulations also allows us to directly compare our results with our saline laboratory experiments at similar bed slopes. A no-slip condition is employed along the bottom boundary, while the free surface is modeled as a stress-free boundary. At the domain outlet, we impose a convective outflow boundary condition that allows the current to exit the domain freely.

2.2. Laboratory Experiment

The laboratory experiments (see Negretti et al., 2017, for more details on the experimental arrangements) were conducted in an open, glass-walled tank 6 m in length connecting two 800-L reservoirs. The channel cross section is 0.25 m wide and 0.2 m deep. The first section of the channel (2 m) is horizontal, permitting the boundary layer of the gravity flow to adjust and fully develop. The next section (3.5 m) consists of a linear slope inclined at an angle of 15°, followed by a flat bed. Pumping salt water with an excess density of 5.6 kg/m^3 from the first reservoir, using an electric agitator to maintain a uniform salt concentration, generated the gravity current. Rhodamine 6G dye was added to the salt water to aid in flow visualization. An outlet at the bottom of the downstream channel was used to control the total water depth and to allow discharge of the lower layer salty flow such that continuous currents could be maintained.

Particle imaging velocimetry was used to measure flow velocity. Polyamide particles with a mean diameter of 60 μm provided tracers, and a 6-W argon-ion laser generated a laser sheet with a width of approximately 1 m and a thickness of 5 mm. Images of 0.7 m by 0.5 m were captured with a time-synchronized charged coupled device (CCD) camera at a rate of 23.8 Hz and a spatial resolution of 0.0435 cm per pixel. The experimental error in the instantaneous velocity is estimated at 3%.

2.3. Field Experiments

Field measurements were collected using Sontek 500-kHz acoustic Doppler current profilers (aDcps; see Kostaschuk et al., 2005, for details), a Nortek acoustic Doppler velocimeter (aDv) and a Sequoia laser in situ sediment transmissometer (LISST-100) that measures both sediment concentration and grain size (Figure 1a). The aDcps were deployed from both moving and moored launches in Lillooet Lake and the Xiaolangdi Reservoir. The Lillooet Lake aDcp data reported herein were collected on 22 August 2001 during a flood on the Lillooet River (see Best et al., 2005, for details), whereas the Xiaolangdi Reservoir measurements were gathered in September 2007 during moderate flow and low suspended sediment conditions in the Huanghe River (Wei, 2010). The aDcps provide 3-D velocity and acoustic backscatter profiles, with backscatter intensity being used to estimate suspended sediment concentrations based on correlations with direct water samples (Kostaschuk et al., 2005) and LISST-100 measurements (Menczel & Kostaschuk, 2013; Wei, 2010). Thermistors and the LISST-100 were used to measure water temperature. Boat positions and aDcp velocity were corrected with real-time kinematic differential global positioning systems that provided a spatial precision to within ±0.1 m.

The aDv and LISST-100 were deployed just offshore of the plunge point in Lillooet Lake in August 2008 during a period of low river flow and sediment concentrations (Figure 1a). This combination of instruments was chosen to examine detailed processes at single points throughout the water column. It was not possible to use the aDcp simultaneously in 2008 because the aDv/LISST-100 deployment interfered with the aDcp beams (see Figure 1a). The aDv was clamped to a fixed structure attached to a rectangular frame that encased the LISST-100 and both were deployed together using a cable and boat-mounted winch. The positions of the LISST-100 and aDv were fixed so that the instruments sampled the flow at the same point in the water column. The LISST-100 and aDv were first lowered to the bed and suspended sediment and velocity data were acquired 0.1 m above the bed for 20 min at a frequency of 1 Hz. The instruments were then raised at

2-m intervals above the bed and the procedure repeated. The drift of the boat was kept at a minimum (±6 m) through the deployment of two anchors: one at the bow of the boat and the other at the stern.

Velocity signals from the aDcps were smoothed using a Gaussian filter to reduce Doppler noise to 0.02 m/s, and the velocity data from the aDv were filtered using a signal-to-noise ratio threshold value of 40, as recommended by the manufacturer. The LISST-100 data were screened for quality by removing all data points greater than five standard deviations from the mean of the total LISST-100 concentration calculated over all 32 bins; this eliminated extreme outliers that sometimes occurred in the larger grain size bins due to detection of coarser material beyond the sampling range of the instrument. Following Chikita (2007), water density was determined from suspended sediment concentration, sediment grain density (assumed = 2,650 kg/m^3), and the density of pure water at the measured water temperature.

2.4. Time Series Analysis

As the velocity measurements in the present study comprise nonstationary data that vary intermittently over time, wavelet analysis (e.g., Torrence & Compo, 1998) was selected to determine any periodicity in the data. Wavelet analysis uses functions called wavelets that are localized in time (Farge, 1992) to show the distribution of variance at different frequencies (or scales), thus decomposing the time series into time-frequency-space (Grinsted et al., 2004; Torrence & Compo, 1998). The Morlet wavelet was chosen for the present analysis because it is nonorthogonal and complex. Nonorthogonal wavelets are best suited for time series analysis when continuous variations in wavelet power are expected, and the Morlet wavelet has been shown to produce fewer artifacts in gravity current data than other wavelet types (Felix et al., 2005). Furthermore, a complex wavelet function that returns information on both amplitude and phase is more useful for capturing oscillatory behavior (Torrence & Compo, 1998).

2.5. Outlet Morphodynamics

We use two dimensionless numbers to summarize conditions at the river mouth outlet. The outlet Reynolds number, Re, is the ratio of inertial forces to viscous forces:

$$\mathrm{Re} = \frac{U_0 h_0}{v}, \tag{1}$$

where U_0 is the mean velocity at the outlet, h_0 is the depth at the outlet, and v is the kinematic viscosity. The outlet Froude Number, Fr, is the ratio of inertial to gravitational forces:

$$Fr = \frac{U_0}{\sqrt{g h_0}}, \tag{2}$$

where g is acceleration due to gravity. For stratified flows at the outlet, such as the DNS and laboratory experiment in this study, modified or reduced gravity $g' = g(\Delta\rho/\rho_2)$ is substituted for g, where $\Delta\rho = \rho_2 - \rho_1$ is the density excess and ρ_1 and ρ_2 are the densities of the lighter and denser fluids, respectively. The resulting numerator in (2), $\sqrt{g' h_0}$, is referred to as the buoyancy velocity U_b.

2.6. Stability Analysis

Dai (2008) used procedures developed by Chakraborty et al. (2006) to examine the length scale, λ, and time scale, τ, of velocity pulsing in Lillooet Lake from surveys conducted in 2001 by Best et al. (2005):

$$\lambda = 4\pi \left(\frac{v_e^2 (\Delta\rho/\rho_1)}{2a} \right)^{1/3}, \tag{3}$$

$$\tau = \left(\frac{2v_e}{a^2 (\Delta\rho/\rho_1)} \right)^{1/3}, \tag{4}$$

where $a = g \sin\theta$ is the acceleration of the current on the delta front slope and v_e is eddy viscosity. The difficulty in these calculations is evaluation of eddy viscosity, which is not readily available from routine measurements, especially in the field (Sumner et al., 2014). Chakraborty et al. (2006) used measured values of the length scale to determine the eddy viscosity from equation (3) and then substituted this value of v_e into (4) to determine the time scale. Herein we follow their procedures.

Table 1
Outlet Conditions

Experiment	Re	Fr
DNS	2,000	0.9*, 0.07
Laboratory	3,500	0.6*, 0.07
Lillooet Lake 22 August 2001	3,440,000	0.05
Xiaolangdi Reservoir	6,275,000	0.07

Note. DNS is direct numerical simulation. Re is the outlet Reynolds number (equation (1)). *Fr* is the outlet Froude number (equation (2)). Note that for the DNS and laboratory *Fr* values marked with an asterisk (*), the reduced gravity is employed because the flow is stratified at the outlet. The nonstratified values of *Fr* for the DNS and laboratory experiment are determined from the velocity and depth of the density currents at the outlet, so as to provide a direct comparison with the field data.

Stratified shear flow instability is examined using the model of Negretti et al. (2008) for inclined flows. Their governing stability equation is

$$\left(\phi_{yy} - \alpha^2 \phi\right) - \frac{u_{yy}}{(u-c)}\phi + J\cos\theta \frac{\rho_y}{(u-c)}\phi \tag{5}$$

$$+ \frac{J\sin\theta}{\iota\alpha(u-c)^2}\left[\rho_{yy}\phi - \frac{\rho_y u_y}{(u-c)}\phi + \rho_y \phi_y\right] = 0,$$

where the subscript y denotes differentiation in the vertical direction, $\alpha = \alpha_r + \iota\alpha_\iota$, α_r is the nondimensional wave number, α_ι is the spatial amplification rate, ϕ is the complex amplitude of the disturbance, $u(y) = b\tanh(y)$ is the nondimensional velocity profile, b is the nondimensional (constant) mean advection, $c = \omega/\alpha$ is the complex wave speed, $\omega = \omega_r + \iota\omega_\iota$, ω_r is the frequency, ω_ι is the temporal amplification rate of the perturbation, J is the bulk Richardson number, $\rho(y) = \tanh(Ry)$ is the nondimensional density profile, and $R = \delta U/\delta\rho$ is the scale ratio of the velocity shear layer thickness δU to the density layer thickness $\delta\rho$ (Figure 1b). Equation (5) reduces to the well-known Taylor-Goldstein equation for horizontal flows when $\theta = 0$. The bulk Richardson number is given by

$$J = \frac{\Delta\rho\, g\, \delta U}{\rho_0 \Delta U^2}, \tag{6}$$

where ρ_0 is the average density of the upper and lower layers and $\Delta U = U_2 - U_1$ is the difference in velocity between the lower layer U_2 and the upper layer U_1 (Figure 1b). The nondimensional wave number is

$$\alpha_r = \frac{2\pi}{\lambda} \frac{\Delta U}{(dU/dy)_{max}}, \tag{7}$$

where $\lambda = \tau_m \overline{u}$ is the wavelength, $\overline{u}$ is the mean convective velocity of the instabilities, τ_m is the measured period of the instabilities, and $(dU/dy)_{max}$ is the maximum velocity gradient in the shear layer (Figure 1b). Negretti et al. (2008) developed stability diagrams based on J, α_r, θ, and R that are used to examine the role of KH instabilities. They found that KH instability regions increase with θ and transition to stable flow occurs at lower J and α_r as R increases.

Although output from the DNS is nondimensional, dimensional values are required for the stability diagram of Negretti et al. (2008). The DNS is laboratory scaled so an outlet depth of $h_0 = 0.1$ m is assigned that is comparable to our laboratory experiment. Combining $h_0 = 0.1$ m with the DNS stratified value of $Fr = 0.9$ at the outlet (Table 1), laboratory density excess $\Delta\rho = 5.6$ kg/m^3 and characteristic density $\rho_0 = 1,001.7$ kg/m^3, equation (2) converts nondimensional DNS velocity U/U_b to U (m/s). We then determine the required values of J, α_r, and R.

3. Results

3.1. DNS

The DNS illustrates the evolution of the gravity current as it passes beyond the river mouth, over the 11° delta front slope and onto the flat lake bed (see Figure 2a and supporting information Movie S1). The simulation shows that the current flowing down the delta front slope has a head and body structure similar to those in classic finite-volume tank experiments (e.g., Middleton, 1993). A small, but stable, zone of reversed flow develops just above the bed immediately downslope of the topographic break that marks the transition from the horizontal river bed to the sloping delta front. A stable plunge point is established quickly at $3x/h_0$ offshore of the river mouth (Figure 2a). The gravity current develops a constant thickness at $5x/h_0$ and a section of downslope propagating, counterclockwise rotating, KH instabilities that persist throughout the simulation extends from $5–1x/h_0$. Time series within this zone (Figure 2b) display remarkably periodic KH billows with thicknesses comparable to the outlet depth and lengths of $1–2x/h_0$.
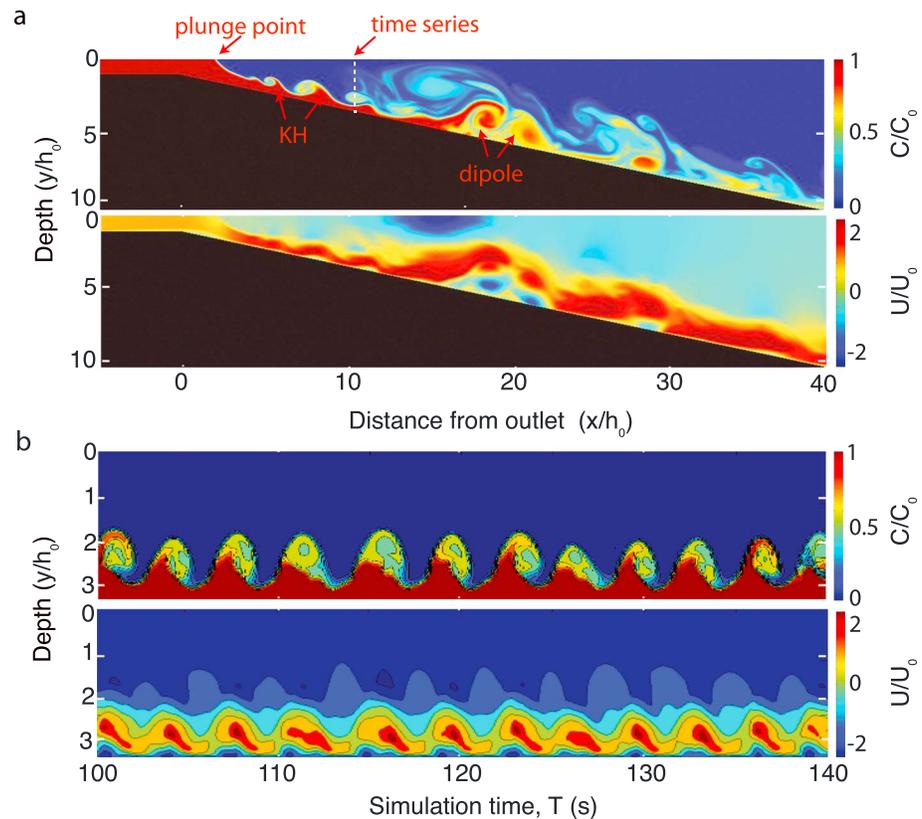
Figure 2. Two-dimensional direct numerical simulation: (a) snapshot of transect at simulation time $T = 33$ s (see supporting information Movie S1) and (b) time series of concentration and streamwise velocity (see supporting information Movie S1) at the time series profile location shown in (a). The flow depth at the outlet h_0 normalizes depth, concentration C is normalized by concentration at the outlet C_0, and the buoyancy velocity at the outlet U_b normalizes velocity. KH = Kelvin-Helmholtz.

Faster-moving KH instabilities begin to override and pair with slower moving vortical structures as the simulation proceeds (cf. vortex pairing of Winant & Browand, 1974; see Figure 2a and supporting information Movie S1), causing larger, compound features that propagate along the entire delta front and onto the lake bed. The vorticity in the bottom boundary layer, which is opposite in sign to the KH vorticity, rolls up into larger vortices. Occasionally, a boundary layer vortex combines with a KH vortex to form a dipole that separates from the bottom boundary. These larger compound features are thicker and have longer wavelengths compared to individual KH structures. As the flow develops and the gravity current entrains ambient fluid, patches of higher density develop, which affect the behavior of subsequent compound flow structures. In some cases, the compound structures ride over the denser patches and develop large eddies that extend upward through a substantial fraction of the water column. Both the transect and the time series show persistent patches of return flow beneath the KH and dipole compound structures, reflecting the influence of local flow separation near the lake bottom (see supporting information Movie S1).

3.2. Laboratory Experiment

The video recording of the laboratory experiment (see supporting information Movie S2) shows that the head of the current reaches the edge of the delta front slope and starts to accelerate as it descends. After an initial unsteady phase associated with the passage of the head, a steady two-layer flow is established (Figure 3a). A thin, stable, accelerating flow develops at the top of the slope to a distance of 0.4 m (Figure 3b) where velocity reaches a critical value and there is an onset of KH billows and enhanced turbulence. Beyond about 0.6 m, the KH billows disappear and are replaced initially by vortex pairs that are subsequently suppressed as turbulence is diminished. The delta-front slope is sufficiently large that the current accelerates again, and
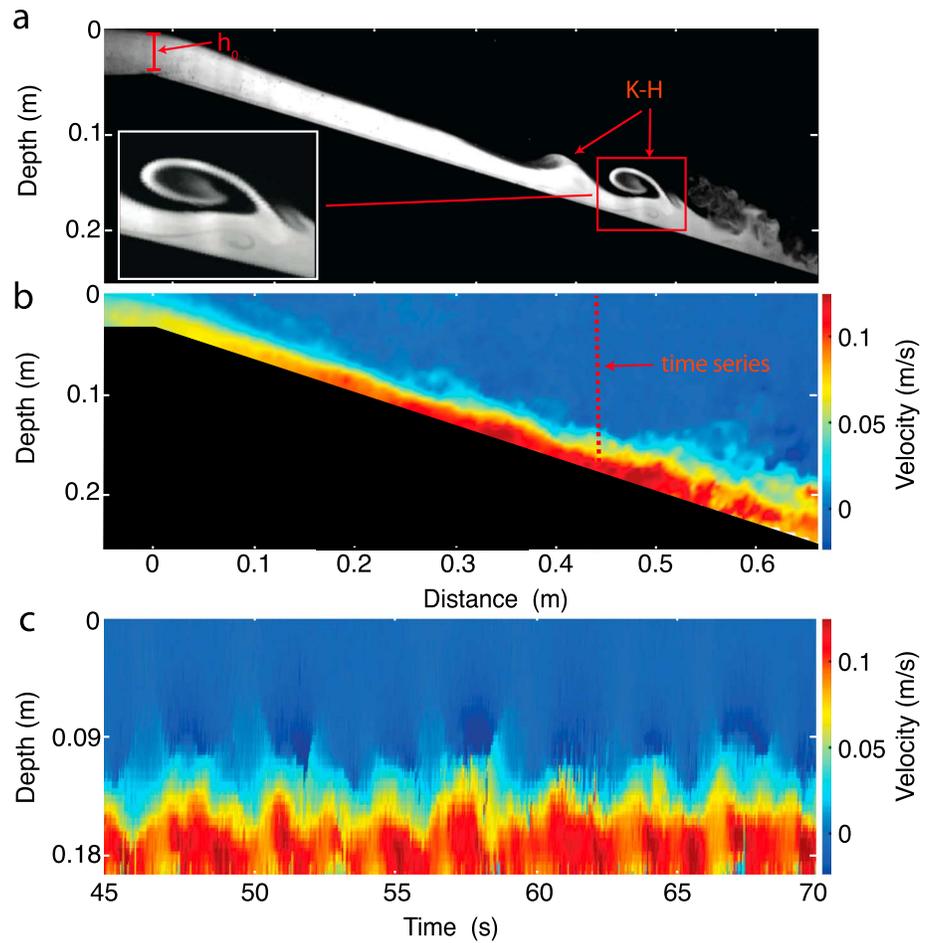
Figure 3. Laboratory saline gravity current: (a) flow visualization at 46 s (see supporting information Movie S2). h_0 is flow depth at the river mouth outlet. The inset shows the occasional dipolar nature of the KH/boundary layer flow. (b) Streamwise velocity at 46 s. (c) Velocity time series at the time series profile location shown in (b). KH = Kelvin-Helmholtz.

further mixing can occur within the already restratified shear layer. Downslope migration of the KH instabilities results in distinct velocity pulses in the time series (Figure 3c).

Secondary vortices generated in the bottom boundary layer of the current rotate in the opposite direction to the primary KH billows (Figure 3a inset). As a KH wave begins to develop, the local velocity below the billow core is directed in the same direction as the flow. At the same time, the depth of the lower layer is reduced so that the flow experiences a rapid increase in velocity close to the bed in response to the buoyancy force and to rotation of the billow. Velocity decreases occur rapidly on the back of the billow, where the depth is larger and the local vertical velocity is directed away from the bed. This enables detachment of the secondary vortex from the bottom boundary. In some cases, the secondary vortices can extend through the entire thickness of the current.

3.3. Field Experiments

Velocity transects from the Xiaolangdi Reservoir reveal several distinct flow zones (Figure 4a). A typical boundary layer (not shown) with an increase in velocity above the bed characterizes flow in the upstream riverine input zone (Wei, 2010), which is followed downstream by a transitional zone where maximum velocity begins to shift downward toward the bed (Figure 4a: 0–700 m). The plunge point marks the position where offshore flow passes beneath the ambient reservoir water and is usually manifested by the accumulation of woody debris. There is no obvious surface lobe at the river mouth, although this could be obscured by the woody debris. The underflow, or turbidity current, develops downstream of the plunge point and there is
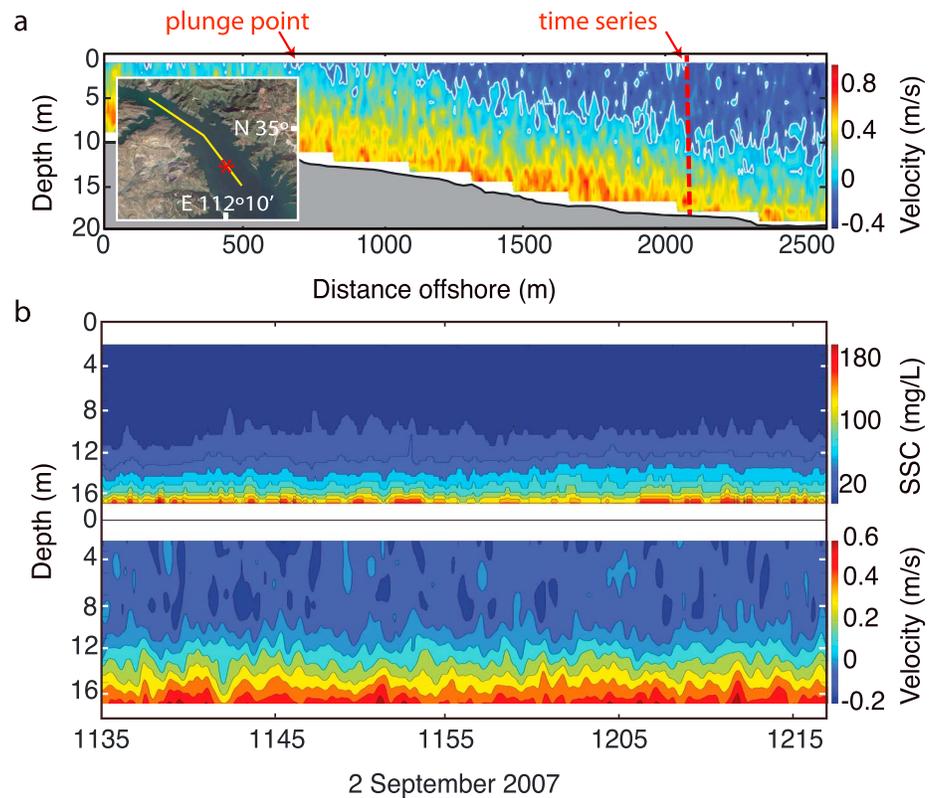
Figure 4. Xiaolangdi Reservoir, China, acoustic Doppler current profiler measurements: (a) streamwise velocity transect. The inset shows the location of the transect (yellow line) and the time series (red star). (b) Time series of streamwise velocity and suspended sediment concentration (SSC) at the locations shown in (a).

a strong upstream return flow. Velocity pulsations are clearly evident in the velocity transect (Figure 4a) and in the sediment concentration and velocity time series (Figure 4b).

The river mouth zone in Lillooet Lake is composed of a nearly horizontal bed and flow vectors within a zone of high sediment concentration that plunges downward at the break-in slope with the steeper 11° delta front (Figure 5a). A distinct surface flow lobe extends offshore in the plunging zone, and velocity vectors shift downward. The return flow of low sediment concentration ambient lake water interacts strongly with the lobe of surface outflow from the river, resulting in a prominent accelerated shear layer that extends toward the bed at the plunge point. The current thins and accelerates below the lobe and then expands offshore into a distinct velocity pulse of about 200 m in length that pinches out near the end of the record. A strong shear layer also occurs at the boundary between the pulse and the ambient lake water. The time series (Figure 5b) of a migrating pulse has a structure similar to that on the transect (Figure 5a) but with a slightly surfaceward flow within the high-concentration zone at the bed and a counterrotating vortex at the boundary with the return flow. The overall return flow in the time series is not as strongly downward as that on the transect and also displays several superimposed small vortices.

3.4. Velocity and Density Profiles

Figure 6 summarizes mean velocity and density profiles from the DNS and laboratory and field experiments. The profiles are averaged over the durations of the time series shown on Figures 2–5. The Lillooet Lake 2008 profiles are more irregular or segmented because they were collected at discrete levels and flow conditions may have changed over the 20-min sampling intervals. Velocity profiles for the DNS, laboratory, and Lillooet Lake 2008 all exhibit clear maxima and then decline toward the bed and surface. The Xiaolangdi Reservoir and Lillooet Lake 2001 profiles were collected with an aDcp so we are unable to measure the lower 1–2 m of the flow close to the bed.
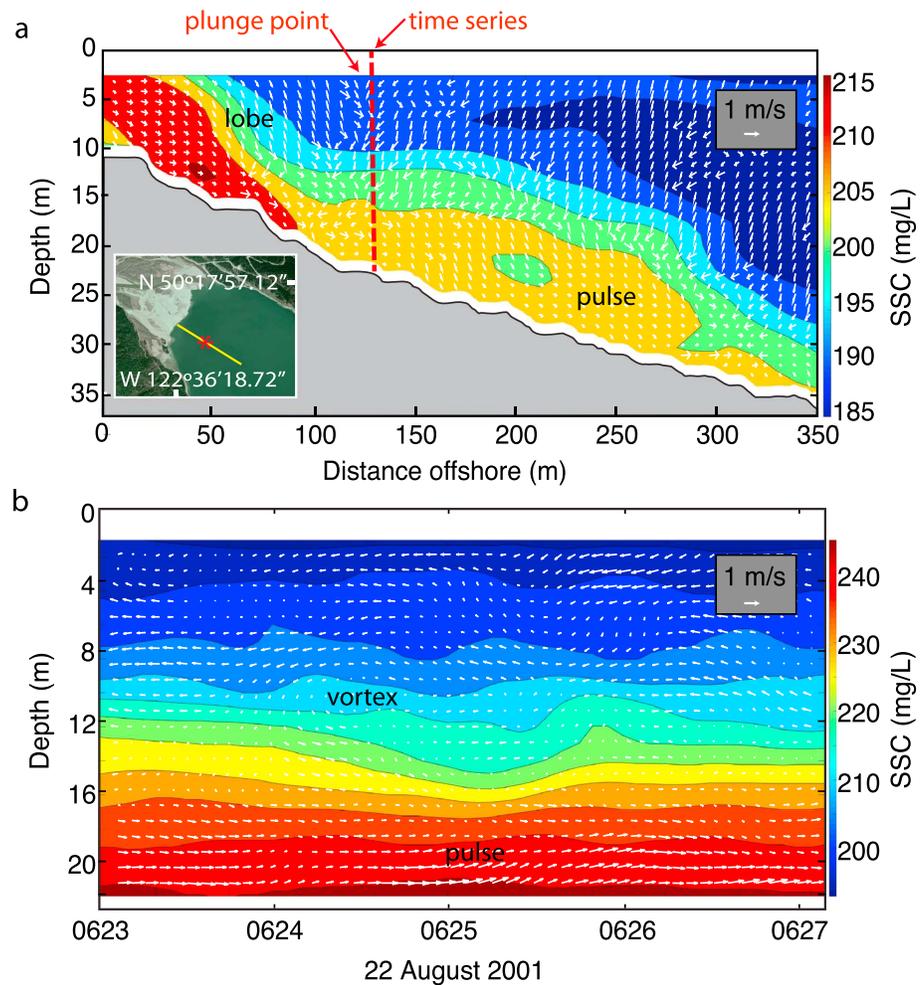
Figure 5. Lillooet Lake acoustic Doppler current profiler measurements: (a) transect and time series (b). The inset in (a) shows the location of the transect (yellow line) and the time series profile (red star). SSC is suspended sediment concentration, and the white arrows are velocity vectors based on streamwise and vertical velocity.

The DNS and laboratory velocity and concentration/density profiles are similar in shape except that the density in the laboratory experiment remains constant further above the bed. The Xiaolangdi Reservoir and Lillooet Lake 2001 profiles also have similar shapes, although the reversed near-surface velocity in Lillooet is much stronger, perhaps due to up-lake wind-driven currents or other circulation patterns in the lake. The gravity current is also much thinner and velocities are higher in Lillooet Lake on 13 August 2008 compared to 14 August 2008, with stronger near-surface return flow on 14 August in response to up-lake winds.

The DNS, Xiaolangdi Reservoir, and Lillooet Lake 2001 velocity and density profiles are not displaced vertically with respect to each other and so are considered symmetric (cf. Lawrence et al., 1991, 2013; Figure 1b). The laboratory velocity profile is clearly displaced above the density profile resulting in asymmetric profiles, and while symmetry is difficult to assess for the irregular Lillooet Lake 2008 profiles, both appear to be slightly asymmetric.

3.5. Wavelet Analysis

The results of wavelet analysis for the velocity time series are presented in Figure 7. The DNS time series is highly periodic and has a distinct and narrow zone of significant and high wavelet power at a period of 3.3 s. The laboratory time series is slightly less periodic but also has narrow zone of significant power at around 2.6 s that extends across the time series. The field time series are more irregular and have a broad
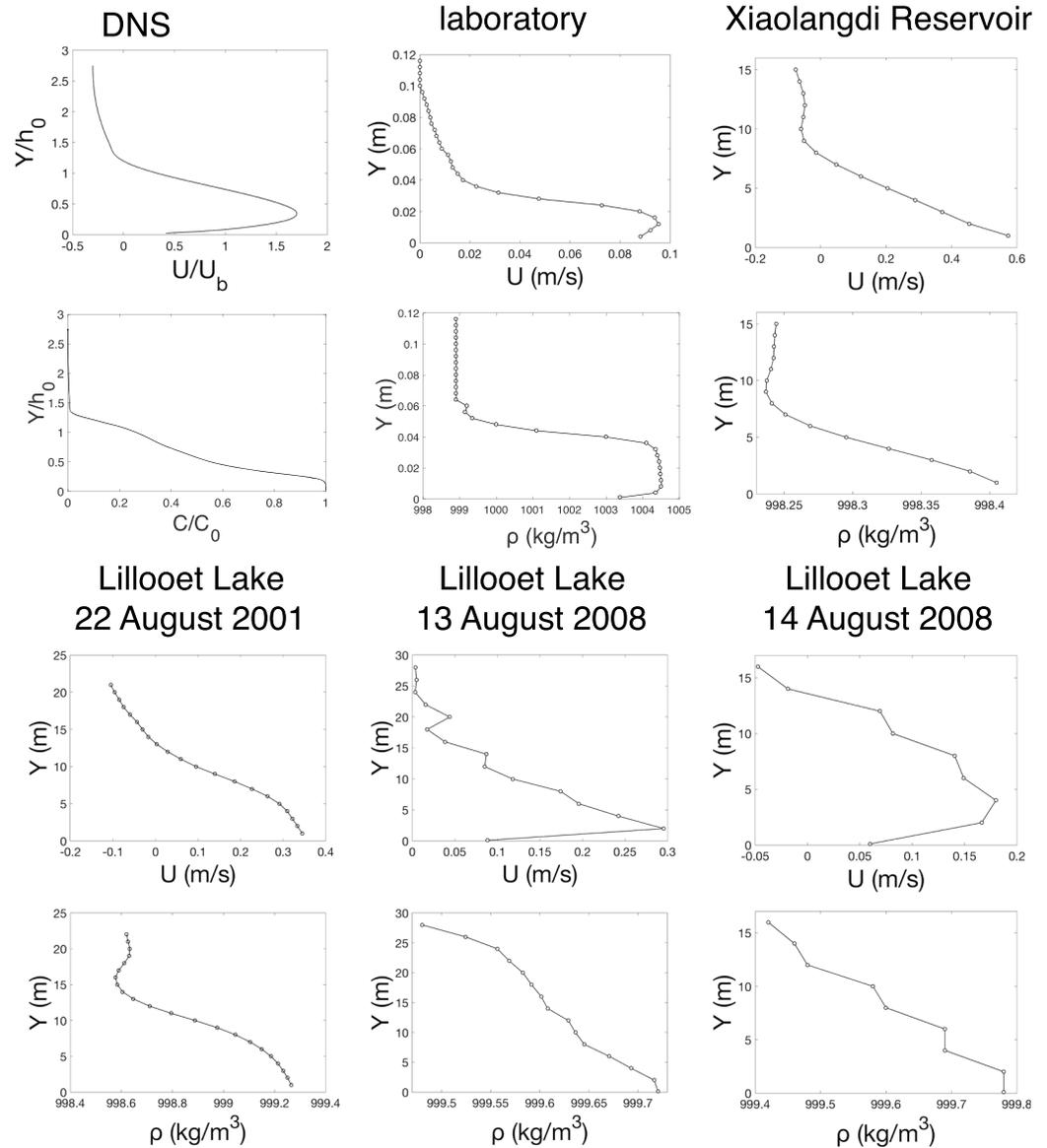
Figure 6. Mean velocity U and density ρ time series profiles for the direct numerical simulation (DNS) and laboratory and field experiments. Locations of the DNS, laboratory, Xiaolangdi Reservoir, and Lillooet Lake 22 August 2001 time series profiles are given on Figures 2–5. For the DNS, velocity is made nondimensional by the buoyancy velocity at the outlet U_b and concentration C is made nondimensional by concentration at the outlet C_0.

range of significant wavelets extending from low to high periods. The power spectrum for Xiaolangdi Reservoir has two distinct periodicities at 150 and 600 s, while for Lillooet Lake 2001, the regions of highest power in the time series are at 300 and 600 s. Time series for Lillooet Lake 2008 are the most irregular of the data set, with the zones of highest spectral power being within the cone of influence and thus are not considered herein. Significant, but weak, periods outside of the cone of influence occur at about 70 s for 13 August and 40 s and 100 s for 14 August.

3.6. Outlet Morphodynamics

Table 1 summarizes outlet morphodynamics for the DNS and laboratory and field experiments. The low values of Re for the DNS and laboratory experiment are representative of conditions found in other laboratory experiments and low-energy mixing events observed in oceans and lakes (e.g., Carpenter et al., 2007). Froude numbers are all comparable and subcritical ($Fr < 1$) at the outlet. Values of Re are more than 3
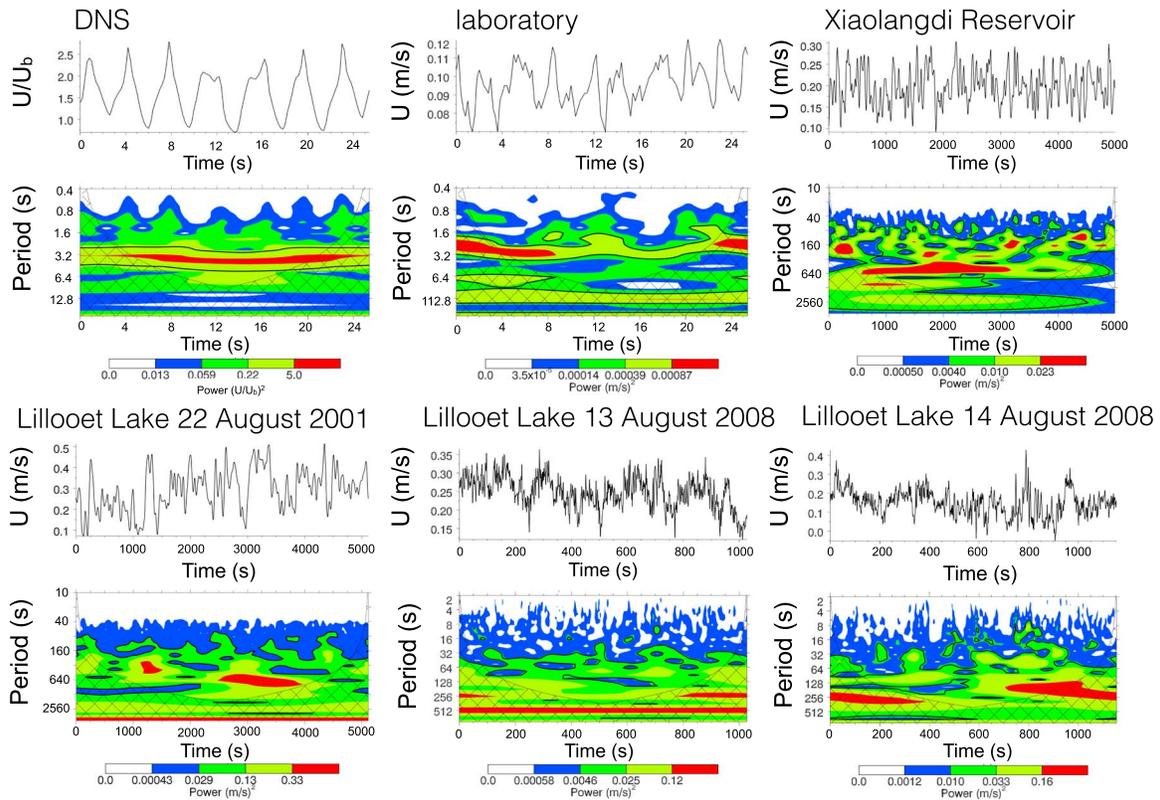
Figure 7. Wavelet analysis of streamwise velocity (U) time series. Locations of the direct numerical simulation (DNS), laboratory, Xiaolangdi Reservoir, and Lillooet Lake 22 August 2001 time series are given on Figures 2–5 and the mean profiles on Figure 6. Time series used for wavelet analysis were taken within the shear layer of each profile, at heights above the bed of $y/h_0 = 0.7$ for the DNS, $y = 0.04$ m for the laboratory, and $y = 5$ m for the Xiaolangdi Reservoir and Lillooet Lake. The DNS and laboratory data were sampled at 5 Hz, the Xiaolangdi Reservoir and Lillooet Lake 2001 at 0.2 Hz, and the laboratory and Lillooet Lake 2008 at 1 Hz. For all experiments the upper panel is the velocity time series and the lower panel is the wavelet power spectrum. Power for the DNS is based on U/U_b and on U for the remaining series. The contour levels are chosen so that 75%, 50%, 25%, and 5% of the wavelet power is above each level, respectively. The cross-hatched region is the cone of influence, where zero padding has reduced the variance. The black contour is the 5% significance level, using a white-noise background spectrum.

orders of magnitude larger for the field compared to the DNS and laboratory. The DNS and laboratory experiments thus have comparable outlet conditions, as do the Lillooet Lake and the Xiaolangdi Reservoir field studies.

3.7. Stability Analysis

Lillooet Lake has distinct river mouth lobes so we expect the RT instability may play a role in pulsing, an expectation supported by the agreement between measured and predicted RT periods for Lillooet Lake (Table 2), particularly the 2008 observations. Lobes are indistinct in Xiaolangdi Reservoir and the predicted RT period is around an order of magnitude larger than the measurements (Table 2), so RT instability is not linked to pulsing. The DNS and laboratory experiments do not have outlet lobes and thus RT predictions (τ_p) are not included in this comparison.

Stability analyses for stratified shear flows, using the model of Negretti et al. (2008), are summarized on Table 2 and Figure 8. Values of the ratio of the shear layer thickness to the density layer thickness are $R \approx 1$ in our experiments, with the exception of the laboratory where $R \approx 2$ (Table 2). Both the bulk Richardson number, J, and nondimensional wave number, α_r, for Lillooet Lake 2008 (Table 2) fall well outside of the critical values for KH instability and are not plotted on Figure 8. For Lillooet Lake 2001, the larger period plots within the KH zone but the smaller period does not. The DNS, laboratory, and Xiaolangdi Reservoir observations all clearly fall within the KH zone.

Table 2
Parameters for Stability Analysis

Experiment	θ (rad)	λ (m)	τ_m (s)	τ_p (s)	J	α_r	R
DNS	0.20	0.35	3.3	—	0.40	0.20	1.13
Laboratory	0.26	0.13	2.6	—	0.38	0.40	2.10
Lillooet Lake 22 August 2001	0.19	68	300	112	0.32	0.95	1.05
		136	600	159		0.48	
Lillooet Lake 13 August 2008	0.12	10	70	73	0.75	3.2	0.87
Lillooet Lake 14 August 2008	0.12	4.5	40	70	0.82	11	1.09
		11	100	112		4.3	
Xiaolangdi Reservoir	0.002	49	150	1,800	0.03	0.90	1.14
		195	600	3,500		0.25	

Note. θ is bed slope, wavelength $\lambda = \tau_m \overline{u}$, τ_m is measured period, $\overline{u}$ is the mean convective velocity of the instabilities (mean velocity of the time series in the shear layer), τ_p is predicted Rayleigh-Taylor period (equation (4)), J is the bulk Richardson number (equation (6)), α_r is the nondimensional wave number (equation (7)), and R is the ratio of the velocity shear layer thickness δU to the density layer thickness $\delta \rho$ (Figure 1b). DNS = direct numerical simulation.

4. Discussion

Here we examine some of the inevitable complexity of the field data, in terms of driving forces, the potential influence of stratification, and the issues surrounding comparison of field data with simulations and experiments undertaken at scales that are orders of magnitude smaller. Subsequently, we discuss evidence for the different pulsation mechanisms and the implications of these in terms of predicting which mechanisms operate in different settings.

4.1. Driving Forces and the Role of Temperature

Normark (1989) found that continuous turbidity currents occur whether lakes are thermally stratified or nearly isothermal, because temperature is thought to contribute little to the density difference between turbidity currents and the ambient lake water. In our laboratory experiment, temperatures are similar in the saline and freshwater tanks so it does not affect density excess. However, the density excess in the saline laboratory current is much larger compared to the field, causing density in the laboratory experiment to remain constant further above the bed (Figure 6; also see Lawrence et al., 2013). Temperatures are similar in the Huanghe River and Xiaolangdi Reservoir (Wei, 2010) and the density excess that drives the turbidity currents is thus mainly due to suspended sediment. In Lillooet Lake in 2001, suspended sediment generated a density excess 0.22 kg/m^3 more than that due to temperature because of high sediment concentrations in Lillooet River. For Lillooet Lake 2008, temperature played a larger role and the density excess for suspended sediment was only ~0.10 kg/m^3 larger than that of temperature.

4.2. Potential Influence of Stratification

Stratification in the receiving water body can complicate the behavior of turbidity currents by splitting them into interflows and underflows (Cortes et al., 2014, 2015; Wells & Nadarajah, 2009), an effect that may influence the turbidity currents in Lillooet Lake during the low river flow in 2008 (Menczel & Kostaschuk, 2013). Large topographic obstacles on the bed can cause the turbidity currents to loft upward (Stevenson & Peakall, 2010) but such obstacles are absent in our study. Density stratification within the currents themselves (Gladstone et al., 2004) can also impact current dynamics and mixing. The Lillooet Lake 2001 turbidity current is the most likely candidate for density stratification because it was generated during a river flood when both fine silt clay and suspended sand were transported to the river mouth. The aDcp data (Figure 5) suggest that
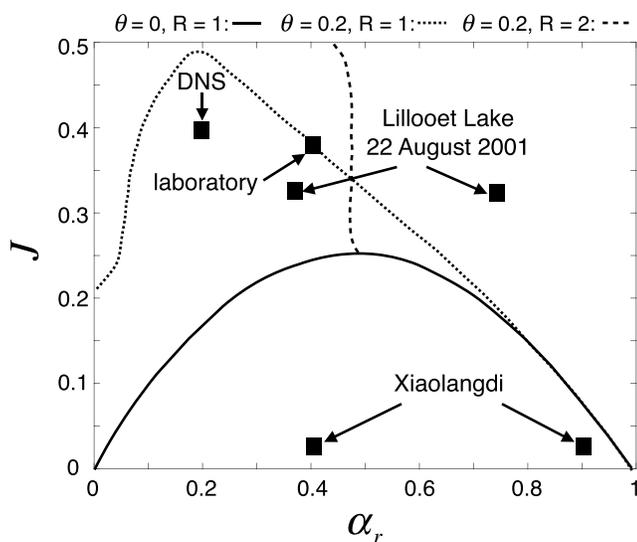

Figure 8. Stability analyses for inclined flows based on data from Table 2. Instability boundaries are from Negretti et al. (2008, their Figures 7 and 10) and separate Kelvin-Helmholtz instability (below the $\theta - R$ lines) and stable flow (above the $\theta - R$ lines). The boundaries are $\theta = 0.2$, $R = 2$ for the laboratory; $\theta = 0.2$, $R = 1$ for Lillooet Lake 22 August 2001 and the direct numerical simulation (DNS); and $\theta = 0$, $R = 1$ for the Xiaolangdi Reservoir.

stratification may be occurring in this current, although the related density profile (Figure 6) is smooth and not *stepped* as would be expected from stratification.

4.3. Spatial Scales and Their Importance

There are significant differences in spatial scales that complicate direct comparisons of offshore transects in the present paper. The Xiaolangdi Reservoir transect, with a river mouth depth $h_0 \sim 10$ m (Figure 4a), covers a depth range from the plunge point of $<2y/h_0$ and an offshore distance of x/h_0 around 150. In comparison, the Lillooet Lake 2001 transect, with $h_0 \sim 12$ m (Figure 5a) spans a depth range of $3.5y/h_0$ and an offshore range of only $35x/h_0$. The thickness of the laboratory gravity current at the mouth is $h_0 \sim 0.06$ m (Figure 3a) so the depth range is $5y/h_0$ with an offshore extent of $12x/h_0$. The DNS transect (Figure 2a) has a depth range of $10y/h_0$ and an offshore distance of $40x/h_0$. The field observations are thus less extensive in terms of the depth scale compared to the laboratory and DNS, and the offshore distance scale for the Xiaolangdi is much larger than the other experiments.

The DNS (Figure 2a) and laboratory (Figure 3a) transects are very similar close to the outlet where the flow accelerates, thins, and then passes basinward into the zone of KH instabilities. This is reflected in similar outlet Reynolds and Froude numbers (Table 1). The lakeward persistence of coherent pulses in the Xiaolangdi Reservoir transect (Figure 4a), however, is much larger than in the laboratory or DNS. Outlet Reynolds numbers, and hence inertial forces, for the Xiaolangdi Reservoir are 3 orders of magnitude larger than the laboratory and DNS cases, so the turbidity current can persist much farther offshore (Table 1).

4.4. Nature of Vortices and Production of Compound Structures

In the laboratory experiment, near-bed secondary vortices develop within individual KH billows (Figure 3a), but these are not obvious in the DNS flows (Figure 2a) or the Lillooet and Xiaolangdi field data (Figures 4a and 5a). In the DNS, the large dipole downslope of the KH zone may develop from secondary vortices, but in this case the structure is much larger than the individual KH billows. The KH zone is also followed downslope by a zone of less well-defined structures in both the laboratory experiment and DNS. These structures, as well as the lower frequency structures in the field, may be related to the compound structures generated in the DNS. Ellison and Turner (1959) describe the compounding of KH instabilities as the "irregular succession of large eddies," which was explained by Turner (1973) as the result of the growth and subsequent overturn or collapse (resembling spirals) of KH instabilities, which in turn produce patches of turbulent mixing. The near-bed return flow beneath the laboratory KH and the compound vortices in the DNS are not evident in the Xiaolangdi or Lillooet Lake 2001 measurements, possibly because the aDcp cannot resolve flow close to the bed. Periodic upslope velocities were recorded in Lillooet Lake near-bed ($y = 0.1$ m) aDv measurements (Figure 6: Lillooet Lake 13 August 2008), even though the mean flow is downslope, suggesting that such flow reversals may exist in the field.

4.5. Velocity Pulsation Mechanisms

The RT analysis (Table 2) indicates that RT instability likely plays a role in velocity pulsing in Lillooet Lake where surface lobes are well developed. The velocity pulse captured on the transect in Lillooet Lake 2001 (Figure 5a) is qualitatively consistent with the RT mechanism (e.g., Dai, 2008) as well. However, the present analysis suggests that RT instability does not play a role in the Xiaolangdi Reservoir, in agreement with the lack of obvious lobes. Importantly, the Xiaolangdi Reservoir also has much lower slopes than Lillooet Lake. Since the period of RT instability is proportional to the inverse square of the acceleration of the current on the delta front slope (equation (4)), the low slope of the Xiaolangdi Reservoir bed results in predicted periods that are much larger than measured (Table 1).

The DNS, laboratory, Xiaolangdi Reservoir, and one of the Lillooet Lake 2001 observations fall within the KH field on Figure 8, but the Lillooet Lake 2008 data do not. Physically, the low velocities of the Lillooet 2008 flows do not generate sufficient shear across the interface necessary to overcome the stabilizing effect of the stratification, so KH waves do not develop. Khavasi et al. (2014) analyzed the stability of particle-laden stratified shear layers and found that large particles make the flow more susceptible to instability. This could affect the Lillooet Lake 2001 current because of possible contributions of suspended sand.

The field data and stability analysis suggest that different types of underflow will be associated with different formative mechanisms for velocity pulsing. Systems with steep slopes, like those with Gilbert-style deltas in

lakes or coarse-grained fan deltas that also exhibit flows with high bulk Richardson numbers, are likely to be dominated by RT instabilities. Systems on lower slopes and with lower bulk Richardson numbers will likely display KH instabilities. This in turn may affect the nature of the initial slope and lead to feedback in the system that reinforces the type of instability. Systems with RT instabilities will undergo increased sedimentation closer to the inlet as a result of repeated growth and decay of lobes and associated movement in the locus of the initial turbidity current, in turn potentially leading to restriction in the development of subaqueous channels (Best et al., 2005). This enhanced sedimentation and lack of topographic confinement will reinforce the development of smooth, steep slopes, thus encouraging further RT instability. In contrast, systems associated with KH instabilities will have relatively lower sedimentation near to source and are more likely to undergo subaqueous channelization (Best et al., 2005), thus reinforcing KH instabilities. Potentially, the two different types of instability help reinforce input systems that tend toward two different topographic end members.

While we have demonstrated an improved understanding of RT and KH instabilities herein, the wide range in significant wavelets in the field time series (Figure 7) suggests that our simple interpretations based on stability analysis of inclined flows must be treated with caution, even though they provide valuable insights into gravity current morphodynamics. There may well be a mix of RT, KH, H, hybrid, and TC instabilities operating simultaneously and at a wide range of scales (e.g., Caulfield et al., 1995), particularly for near-horizontal flows such as the Xiaolangdi Reservoir.

5. Conclusions

Velocity pulsing is ubiquitous in continuous, natural turbidity currents in Lillooet Lake and the Xiaolangdi Reservoir. Pulses have been attributed to RT instability generated by sinking surface lobes along the plunge line where the river enters the receiving water body, and to interfacial waves along the underflow such as KH instability. DNSs and laboratory experiments provide details on the dynamics of KH instabilities and their amalgamation. Stability analyses for inclined flows suggest that velocity pulsing in the DNS, laboratory, and Xiaolangdi Reservoir is due to KH instability, whereas RT instability contributes to pulsing in Lillooet Lake. Interpretations of the causes of pulsing in geophysical flows must be treated with caution, however, because of difficulties in collecting and interpreting field measurements where a wide range of processes may be operating simultaneously at many spatial and temporal scales. Velocity pulsing however is clearly a fundamental component of continuous turbidity currents and must be incorporated into models of their behavior.

The results from field measurements, including Lillooet Lake and the Xiaolangdi Reservoir, are limited to a few positions and fail to capture the full spatial evolution of turbidity currents. A fully 3-D field study of natural turbidity currents could be accomplished using the water column capabilities of multibeam echo sounders, as described by Best et al. (2010). Multibeam echo sounders can provide detailed visualizations of suspended sediment concentrations and velocity and reveal the temporal evolution and growth of instabilities along mixing interfaces. Multibeam echo sounders also enable high-precision bathymetric mapping that would enhance understanding of the relationship of turbidity currents and bed morphology.

References

Azpiroz-Zabala, M., Cartigny, M. J. B., Talling, P. J., Parsons, D. R., Sumner, E. J., Clare, M. A., et al. (2017). Newly recognized turbidity current structure can explain prolonged flushing of submarine canyons. *Science Advances*, *3*(10), e1700200. https://doi.org/10.1126/sciadv.1700200

Best, J. L., Kostaschuk, R. A., Peakall, J., Villard, P. V., & Franklin, M. (2005). Whole flow field dynamics and velocity pulsing within natural sediment-laden underflows. *Geology*, *33*(10), 765–768. https://doi.org/10.1130/G21516.1

Best, J. L., Simmons, S., Parsons, D. R., Oberg, K., Czuba, J., & Malzone, C. (2010). A new methodology for the quantitative visualization of coherent flow structures in alluvial channels using multibeam echo-sounding (MBES). *Geophysical Research Letters*, *37*, L06405. https://doi.org/10.1029/2009GL041852

Bradford, S. F., Katopodes, N. D., & Parker, G. (1997). Characteristic analysis of turbid underflows. *Journal of Hydraulic Engineering*, *123*(5), 420–431. https://doi.org/10.1061/(ASCE)0733-9429(1997)123:5(420)

Brown, G. L., & Roshko, A. (1974). On density effects and large structure in turbulent mixing layers. *Journal of Fluid Mechanics*, *64*(04), 775–816. https://doi.org/10.1017/S002211207400190X

Carpenter, J. R., Balmforth, N. J., & Lawrence, G. A. (2010). Identifying unstable modes in stratified shear layers. *Physics of Fluids*, *22*(5), 054104. https://doi.org/10.1063/1.3379845

Carpenter, J. R., Lawrence, G. A., & Smyth, W. D. (2007). Evolution and mixing of asymmetric Holmboe instabilities. *Journal of Fluid Mechanics*, *582*, 103–132. https://doi.org/10.1017/S0022112007005988

Carpenter, J. R., Tedford, E. W., Heifetz, E., & Lawrence, G. A. (2011). Instability in stratified shear flow: Review of a physical interpretation based on interacting waves. *Applied Mechanics Reviews*, *64*, 060801.

Caulfield, C., Peltier, W., Yoshida, S., & Ohtani, M. (1995). An experimental investigation of the instability of a shear flow with multilayered density stratification. *Physics of Fluids*, *7*(12), 3028–3041. https://doi.org/10.1063/1.868679

Chakraborty, P., Gioia, G., & Kieffer, S. (2006). Volcan Reventador's unusual umbrella. *Geophysical Research Letters*, *33*, L05313. https://doi.org/10.1029/2005GL024915

Chikita, K. (2007). Topographic effects on the thermal structure of Himalayan glacial lakes: Observations and numerical simulation of wind. *Journal of Asian Earth Sciences*, *30*(2), 344–352. https://doi.org/10.1016/j.jseaes.2006.10.005

Cortes, A., Rueda, F. J., & Wells, M. G. (2014). Experimental observations of the splitting of a gravity current at a density step in a stratified water body. *Journal of Geophysical Research: Oceans*, *119*, 1038–1053. https://doi.org/10.1002/2013JC009304

Cortes, A., Wells, M. G., Fringer, O. B., Arthur, R. S., & Rueda, F. J. (2015). Numerical investigation of split flows by gravity currents into two-layered stratified water bodies. *Journal of Geophysical Research: Oceans*, *120*, 5254–5271. https://doi.org/10.1002/2015JC010722

Cossu, R., Forrest, A. L., Roop, H. A., Dunbar, G. B., Vandergoes, M. J., Levy, R. H., et al. (2015). Seasonal variability in turbidity currents in Lake Ohau, New Zealand and their influence on sedimentation. *Marine and Freshwater Research*, *67*(11), 1725–1739. https://doi.org/10.1071/MF15043

Crookshanks, S., & Gilbert, R. (2008). Continuous, diurnally fluctuating turbidity currents in Kluane Lake, Yukon Territory. *Canadian Journal of Earth Sciences*, *45*(10), 1123–1138. https://doi.org/10.1139/E08-058

Dai, A. (2008). Analysis and modeling of plunging flows, (Doctoral Dissertation). Urbana-Champaign, IL: University of Illinois.

De Cesare, G., Schleiss, A., & Hermann, F. (2001). Impact of turbidity currents on reservoir sedimentation. *Journal of Hydraulic Engineering*, *127*(1), 6–16. https://doi.org/10.1061/(ASCE)0733-9429(2001)127:1(6)

De Cesare, G. A., Boillat, J. L., & Schleiss, A. J. (2006). Circulation in stratified lakes due to flood-induced turbidity currents. *Journal of Environmental Engineering*, *132*(11), 1508–1517. https://doi.org/10.1061/(ASCE)0733-9372(2006)132:11(1508)

Desloges, J. R., & Gilbert, R. (1994). Sediment source and hydroclimatic inferences from glacial Lake sediments: The post-glacial sedimentary record of Lillooet Lake, British Columbia. *Journal of Hydrology*, *159*(1-4), 375–393. https://doi.org/10.1016/0022-1694(94)90268-2

Eadie, B. J., Schwab, D., Johengen, T., Lavrentyev, P., Miller, G., Holland, R., et al. (2002). Particle transport, nutrient cycling, and algal community structure associated with a major winter-spring sediment resuspension event in southern Lake Michigan. *Journal of Great Lakes Research*, *28*(3), 324–337. https://doi.org/10.1016/S0380-1330(02)70588-1

Ellison, T. H., & Turner, J. S. (1959). Turbulent entrainment in stratified flows. *Journal of Fluid Mechanics*, *6*(03), 423–448. https://doi.org/10.1017/S0022112059000738

Farge, M. (1992). Wavelet transforms and their applications to turbulence. *Annual Review of Fluid Mechanics*, *24*(1), 395–458. https://doi.org/10.1146/annurev.fl.24.010192.002143

Felix, M., Sturton, S., & Peakall, J. (2005). Combined measurements of velocity and concentration in experimental turbidity currents. *Sedimentary Geology*, *179*(1-2), 31–47. https://doi.org/10.1016/j.sedgeo.2005.04.008

Gilbert, R. (1975). Sedimentation in Lillooet Lake. *Canadian Journal of Earth Sciences*, *12*(10), 1697–1711. https://doi.org/10.1139/e75-151

Gilbert, R., Crookshanks, S., Hodder, K. R., Spagnol, J., & Stull, R. B. (2006). The record of an extreme flood in the sediments of montane Lillooet Lake, British Columbia: Implications for paleoenvironmental assessment. *Journal of Limnology*, *35*, 737–745.

Gladstone, C., Ritchie, L. J., Sparks, R. S. J., & Woods, A. W. (2004). An experimental investigation of density-stratified inertial gravity currents. *Sedimentology*, *51*(4), 767–789. https://doi.org/10.1111/j.1365-3091.2004.00650.x

Grinsted, A., Moore, J. C., & Jevrejeva, S. (2004). Application of the cross wavelet transform and wavelet coherence to geophysical time series. *Nonlinear Processes in Geophysics*, *11*(5/6), 561–566. https://doi.org/10.5194/npg-11-561-2004

Guha, A., & Lawrence, G. A. (2014). A wave interaction approach to studying non-modal homogenous and stratified shear instabilities. *Journal of Fluid Mechanics*, *755*, 336–364. https://doi.org/10.1017/jfm.2014.374

Hsu, K. J., & Kelts, K. (1985). Swiss lakes as a geological laboratory. Part I: Turbidity currents. *Naturwissenschaften*, *72*(6), 315–321. https://doi.org/10.1007/BF00454774

Khavasi, E., Firoozabadi, B., & Afshin, H. (2014). Linear analysis of the stability of particle-laden stratified shear layers. *Canadian Journal of Physics*, *92*(2), 103–115. https://doi.org/10.1139/cjp-2013-0028.

Kostaschuk, R. A., Best, J. L., Villard, P. V., Peakall, J., & Franklin, M. (2005). Measuring flow velocity and sediment transport with an acoustic Doppler current profiler. *Geomorphology*, *68*(1-2), 25–37. https://doi.org/10.1016/j.geomorph.2004.07.012

Lamb, M. P., McElroy, B., Kopriva, B., Shaw, J., & Mohrig, D. (2010). Linking river-flood dynamics to hyperpycnal-plume deposits: Experiments, theory, and geological implications. *Geological Society of America Bulletin*, *122*(9-10), 1389–1400. https://doi.org/10.1130/B30125.1

Lamb, M. P., & Mohrig, D. (2009). Do hyperpycnal-flow deposits record river-flood dynamics? *Geology*, *37*(12), 1067–1070. https://doi.org/10.1130/G30286A.1

Lambert, A. M., & Luthi, S. M. (1977). Lake circulation induced by density currents: An experimental approach. *Sedimentology*, *2*, 735–741.

Lawrence, G. A., Browand, F., & Redekopp, L. (1991). The stability of a sheared density interface. *Physics of Fluids*, *3*(10), 2360–2370. https://doi.org/10.1063/1.858175

Lawrence, G. A., Tedford, E. W., & Carpenter, J. R. (2013). Instabilities in stratified shear flow. In J. G. Venditti, J. L. Best, M. Church, & R. J. Hardy (Eds.), *Coherent flow structures at Earth's surface* (1st ed., pp. 237–271). Chichester, UK: John Wiley. https://doi.org/10.1002/9781118527221.ch5

Meiburg, E., & Kneller, B. (2010). Turbidity currents and their deposits. *Annual Review of Fluid Mechanics*, *42*(1), 135–156. https://doi.org/10.1146/annurev-fluid-121108-145618

Menczel, A., & Kostaschuk, R. (2013). Interfacial waves as coherent flow structures associated with continuous turbidity currents: Lillooet Lake, Canada. In J. G. Venditti, J. L. Best, M. Church, & R. J. Hardy (Eds.), *Coherent flow structures at Earth's surface* (1st ed., pp. 371–383). Chichester, UK: John Wiley.

Middleton, G. V. (1993). Sediment deposition from turbidity currents. *Annual Review of Earth and Planetary Sciences*, *21*(1), 89–114. https://doi.org/10.1146/annurev.ea.21.050193.000513

Mittal, R., & Iaccarino, G. (2005). Immersed boundary methods. *Annual Review of Fluid Mechanics*, *37*(1), 239–261. https://doi.org/10.1146/annurev.fluid.37.061903.175743

Nasr-Azadani, M. M., Hall, B., & Meiburg, E. (2013). Polydisperse turbidity currents propagating over complex topography: Comparison of experimental and depth-resolved simulation results. *Computers & Geosciences*, *53*, 141–153. https://doi.org/10.1016/j.cageo.2011.08.030

Nasr-Azadani, M. M., & Meiburg, E. (2011). TURBINS: An immersed boundary, Navier–Stokes code for the simulation of gravity and turbidity currents interacting with complex topographies. *Computers and Fluids*, *45*(1), 14–28. https://doi.org/10.1016/j.compfluid.2010.11.023

Nasr-Azadani, M. M., & Meiburg, E. (2014a). Turbidity currents interacting with three-dimensional seafloor topography. *Journal of Fluid Mechanics*, *745*, 409–443. https://doi.org/10.1017/jfm.2014.47

Nasr-Azadani, M. M., & Meiburg, E. (2014b). Influence of seafloor topography on the depositional behavior of bi-disperse turbidity currents: A three-dimensional, depth-resolved numerical investigation. *Environmental Fluid Mechanics*, *14*(2), 319–342. https://doi.org/10.1007/s10652-013-9292-5

Necker, F., Härtel, C., Kleiser, L., & Meiburg, E. (2002). High-resolution simulations of particle-driven gravity currents. *International Journal of Multiphase Flow*, *28*(2), 279–300. https://doi.org/10.1016/S0301-9322(01)00065-9

Negretti, M. E., Flor, J. B., & Hopfinger, E. J. (2017). Development of gravity currents on rapidly changing slopes. *Journal of Fluid Mechanics*, *833*, 70–97. https://doi.org/10.1017/jfm.2017.696

Negretti, M. E., Socolofsky, S. A., & Jirka, G. H. (2008). Linear stability analysis of inclined two-layer stratified flows. *Physics of Fluids*, *20*(9), 094104. https://doi.org/10.1063/1.2980351

Normark, W. R. (1989). Observed parameters for turbidity-current flow in channels, Reserve Fan, Lake Superior. *Journal of Sedimentary Petrology*, *59*, 423–431.

Smyth, W. D., Carpenter, J. R., & Lawrence, G. A. (2007). Mixing in symmetric Holmboe waves. *Journal of Physical Oceanography*, *37*(6), 1566–1583. https://doi.org/10.1175/JPO3037.1

Smyth, W. D., & Winters, K. B. (2003). Turbulence and mixing in Holmboe waves. *Journal of Physical Oceanography*, *33*(4), 694–711. https://doi.org/10.1175/1520-0485(2003)33<694:TAMIHW>2.0.CO;2

Stevenson, C. J., & Peakall, J. (2010). Effects of topography on lofting gravity flows: Implications for the deposition of deep-water massive sands. *Marine and Petroleum Geology*, *27*(7), 1366–1378. https://doi.org/10.1016/j.marpetgeo.2010.03.010

Sumner, E. J., Peakall, J., Dorrell, R. M., Parsons, D. R., Darby, S. E., Wynn, R. B., et al. (2014). Driven around the bend: Spatial evolution and controls on the orientation of helical bend flow in a natural submarine gravity current. *Journal of Geophysical Research: Oceans*, *119*, 898–913. https://doi.org/10.1002/2013JC009008

Taylor, G. (1931). Effect of variation in density on the stability of superposed streams of fluid. *Proceedings of the Royal Society of London A*, *132*(820), 499–523. https://doi.org/10.1098/rspa.1931.0115

Torrence, C., & Compo, G. (1998). A practical guide to wavelet analysis. *Bulletin of the American Meteorological Society*, *79*(1), 61–78. https://doi.org/10.1175/1520-0477(1998)079<0061:APGTWA>2.0.CO;2

Turner, J. S. (1973). *Buoyancy effects in fluids*. Cambridge, UK: Cambridge University Press. https://doi.org/10.1017/CBO9780511608827

Wei, T. (2010). The effects of positive gradient breaks on flow and sediment dynamics in density currents, (Doctoral Dissertation). Leeds, UK: University of Leeds.

Wei, T., Peakall, J., Parsons, D. R., Chen, Z., Zhao, B., & Best, J. L. (2013). Three-dimensional gravity-current flow within a subaqueous bend: Spatial evolution and force balance variations. *Sedimentology*, *60*(7), 1668–1680. https://doi.org/10.1111/sed.12052

Weirich, F. H. (1986). The record of density-induced underflows in a glacial lake. *Sedimentology*, *33*(2), 261–277. https://doi.org/10.1111/j.1365-3091.1986.tb00535.x

Wells, M. G., & Nadarajah, P. (2009). The intrusion depth of density currents flowing into stratified water bodies. *Journal of Physical Oceanography*, *39*(8), 1935–1947. https://doi.org/10.1175/2009JPO4022.1

Winant, C. D., & Browand, F. K. (1974). Vortex pairing: The mechanism of turbulent mixing-layer growth at moderate Reynolds number. *Journal of Fluid Mechanics*, *63*(02), 237–255. https://doi.org/10.1017/S0022112074001121